# Image correction scheme applied to functional diffuse optical tomography scattering images

Harry L. Graber, Yong Xu, and Randall L. Barbour

We have extended our investigation on the use of a linear algorithm for enhancing the accuracy of diffuse optical tomography (DOT) images, to include spatial maps of the diffusion coefficient. The results show that the corrected images are markedly improved in terms of estimated size, spatial resolution, two-object resolving power, and quantitative accuracy. These image-enhancing effects are significant at expected levels of diffusion-coefficient contrast in tissue and noise levels typical of experimental DOT data. Overall, the types and magnitudes of image-enhancing effects obtained here are qualitatively similar to those seen in previous studies on $\mu_a$ perturbations. The implications for practical implementations of DOT time-series imaging are discussed. 

*OCIS codes:* 100.1830, 100.2980, 100.6950, 170.3010, 170.3880.

## 1. Introduction

Three factors common to all forms of functional imaging are needed for system hardware, algorithms for image formation, and feature-extraction methods. In the case of dynamic DOT studies, a particular challenge is to develop image-formation algorithms that are robust to experimental uncertainties, and are computationally efficient. In prior reports we have shown that while the normalized difference method (NDM) meets these requirements,[1] it can produce images that have reduced resolution and added spatial bias (particularly, in limited-view cases) compared to the much more computationally intensive iterative recursive methods.[2]

In a series of reports, we have described a linear image-correction algorithm that is both computationally efficient and can substantially improve the image quality produced by the NDM method.[3–6] This correction is computed by a method motivated by the principles of magnetic resonance imaging, which uses a spatial gradient in the Larmor frequency to encode position information.[7] In our case, by encoding each pixel location with a unique temporal signature, it becomes possible to directly identify the contributions of all parts of a medium to each image pixel.[3] Then the inverse of the medium-to-image mapping can be used to reapportion recovered optical coefficient values to their correct locations.[4,5] As shown in this paper, this technique can be successfully applied to complex tissue backgrounds, and it is effective even in the absence of anatomical priors.[8] In previous reports, the image correction algorithm was applied to media having inhomogeneity in the absorption coefficient only. Here we extend our investigations to include media with spatially heterogeneous scattering coefficients.

## 2. Methods

### A. Target Medium Structure and Optical Properties

Figure 1 shows the geometry and source-detector arrangement used to generate the simulated data. A 2D circular medium 8 cm in diameter, and full tomographic measurements with 32 sources and 32 collocated D, were modeled. The background medium was homogeneous and static, with $\mu_a^{\text{bkgr}} = 0.06$ $\text{cm}^{-1}$ and $\mu_s'^{\text{bkgr}} = 10$ $\text{cm}^{-1}$. Either one or two circular inclusions were introduced, whose position and size were varied as described below, and whose scattering properties were varied sinusoidally in time at frequencies within the vasomotor region ($<0.15$ Hz). Two levels of contrast were considered. In the low-contrast case, the mean value of the time-varying scattering was equal to the background value, with 10% modulation amplitude. The modulation fre-

The authors are with the Department of Pathology, State University of New York Downstate Medical Center, Box 25, 450 Clarkson Avenue, Brooklyn, New York 11203. H. Graber's e-mail address is harry.graber@downstate.edu.

Received 12 July 2006; revised 16 November 2006; accepted 27 November 2006; posted 30 November 2006 (Doc. ID 72864); published 13 March 2007.

0003-6935/07/101705-12$15.00/0

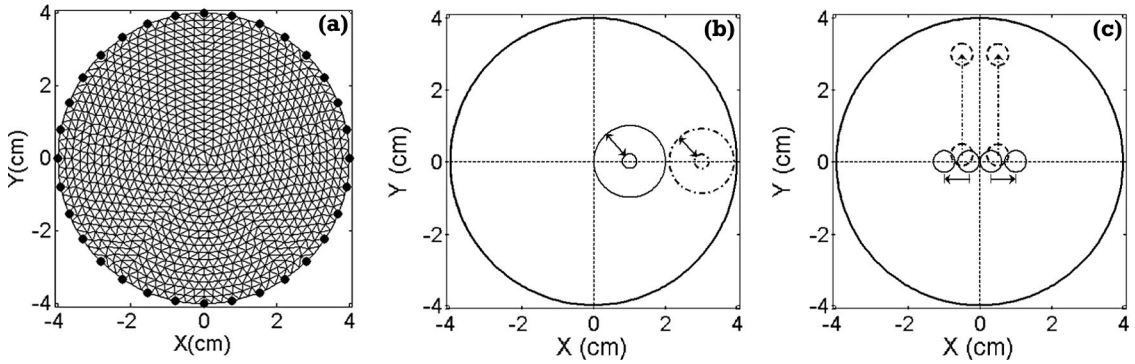


Fig. 1. Model specifications for DOT forward problem. (a) FEM mesh (981 nodes) used for all inverse-problem computations, with the locations of the isotropic point sources and detectors on the boundary also indicated. (b) Inclusion locations and size ranges modeled in single-inclusion studies. The center was placed at either $(x_c, y_c) = (1, 0)$ (solid circles) or $(x_c, y_c) = (3, 0)$ (dot-dashed circles). Smallest (0.4 cm diam.) and largest (1.8 or 2.0 cm diam.) inclusion sizes are shown. (c) Inclusion locations modeled in two-inclusion studies. Solid circles and arrows indicate the range of positions used in the fixed $y_c$, increasing $x_c$ study. Dashed circles and arrows indicate the range of positions used in the fixed $x_c$, increasing $y_c$ study.

quency was $f = 0.02$ Hz for single inclusion studies, and $f = 0.02$ and 0.05 Hz for two-inclusion studies. In the case of high contrast, the mean value of the temporal function was either two or three times the background $\mu_s'$, with 20% modulation amplitude, and $f = 0.1$ Hz for both the one- and two-inclusion studies.

The inclusion size and position were adjusted in an effort to explore the known position-dependent spatial blurring and bias associated with first-order reconstructions (i.e., poorer spatial resolution at greater depths and increased bias at intermediate depths) of $\mu_a$.[5] In the case of a single object, the radius was varied from a minimum of 0.2 cm to a maximum of either 1.0 cm (deep inclusion) or 0.9 cm (superficial inclusion). The center positions and size ranges modeled are indicated in Fig. 1(b). For the two-object case, two different positional studies were performed. In both studies the object sizes were fixed, with a radius of 0.3 cm. The depth dependence of resolution was explored by varying the location of the inclusion pair from the center to a minimum depth of 1 cm in increments of 0.2 cm. Resolving power about the medium's center was evaluated by varying the center-to-center distance between the pair from 0.6 cm (i.e., objects in contact) to 2.0 cm. Dynamic behavior was modeled over a 50 s time period, with a 0.5 s sampling interval.

### B. Forward Problem

All surface detector data and internal photon intensities computed for target and reference media were obtained by solving the diffusion equation with Robin boundary conditions[1,9] using the finite element method (FEM). These were computed using two different mesh densities. For target media a heterogeneous fine mesh was used (2593–2670 nodes, depending on target details). Reference-medium computations were made using a homogeneous coarse mesh (981 nodes) having the same background optical properties as the target media. The same coarse mesh was also used to compute the image correction matrices and for the inverse problem. The number of time frames modeled for the dynamic targets and for the image correction matrix were 100 and $2^{14}$, respectively. The latter required approximately 1.5 h to compute on a 2.8 GHz PC, while the former took less than 5 min.

### C. Inverse Problem

The images were reconstructed by using the NDM,[1] which computes images of $\Delta\mu_a$ and $\Delta D$ with respect to a defined reference medium. For the computational studies considered here, we found that it was not necessary to employ a fine-onto-coarse mesh interpolation scheme such as that of Ref. 8. The coarse mesh shown in Fig. 1(a) is sufficiently dense that the computed FEM solutions are good approximations of analytic solutions to the continuous diffusion equation.

The images produced by using the NDM were corrected by applying the linear correction algorithm described in Refs. 3–6 and Ref. 8. The primary difference between the previous correction-matrix computations and that undertaken for this report is that here $\mu_s'$, rather than $\mu_a$, was modulated in each reference-medium pixel. All modeled $\Delta\mu_s'(x, y)$ states were converted to the corresponding spatial distributions of $\Delta D$, and the correction matrix was generated by comparing the latter to the recovered $\Delta D$ images, as set forth in Refs. 3–5.

The effects of random error were explored by introducing additive Gaussian white noise, at levels of 1%, 2%, 3%, 5%, and 8% (only the first three are used in the two-inclusion case). Here the noise level $\varepsilon_k$ for the $k$th S-D channel is defined as $\varepsilon_k = 100 s_k / m_k^0$, $s_k$ is the standard deviation of the $k$th channel noise distribution, and $m_k^0$ is the time-averaged noise-free detector reading.

Using the same PC as for forward problems, the computation time was approximately 20 min for the $2^{14}$ correction-operator inverse problems, while each set of 100 target-medium inverse problems required less than 1 min. Image correction, which involves nothing more than one additional matrix multiplication,[3–5] took less than a second.

### D. Noise Suppression

Recovered images were postprocessed with a noise-suppression scheme that combines temporal low-pass filtering (tLPF) and spatial pillbox filtering (sLPF), as described in Refs. 6 and 8. The effects of this procedure were quantified by computing the spatial and temporal accuracies of the images before and after filtering.

### E. Quantification of Image Accuracy

The spatial and temporal correlation coefficients (SC and TC, respectively), and spatial and temporal root-mean-squared difference (sRMSD and tRMSD, respectively), between target medium and reconstructed images are used here as global indices of spatial and temporal accuracies of recovered images.[6] The SC (ideal value is 1.0), being amplitude independent, quantifies qualitative accuracy, while an RMSD (ideal value is 0.0) is a measure of quantitative accuracy.[10]

In addition, four local accuracy measures were computed. These include the contrast and FWHM of the recovered inclusion, and, in the case of two-inclusion studies, measures of the between-object resolving power and location bias. Resolving power, $P_d$, was defined as the depth of the notch between the recovered inclusions (Fig. 2), relative to the ideal depth. Mathematically

$$P_d = \frac{\Delta(\delta D)}{\delta D_0}, \tag{1}$$

where $\delta D = D^{\mathrm{bkgr}} - D^{\mathrm{incl}}$, $\delta D_0$ is the maximal value of $\delta D$, and $\Delta(\delta D)$ is the difference between $\delta D_0$ and the $\delta D$ value at a mesh node halfway between the inclusions. The location bias, $P_s$, was measured by computing the distance between the recovered inclusions, relative to the ideal separation. That is

$$P_s = \frac{\delta X}{\delta X_0}, \tag{2}$$

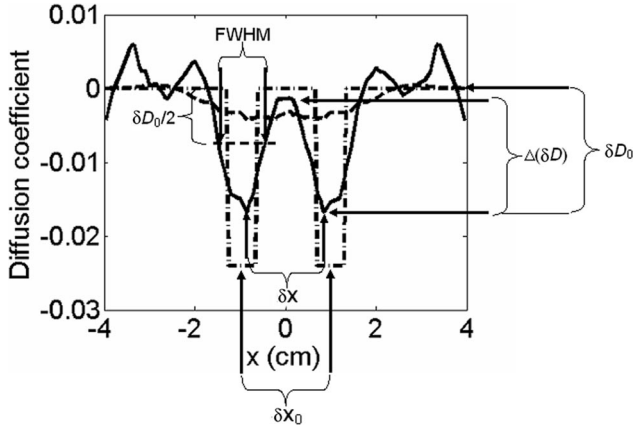


Fig. 2. Definitions of several parameters used in calculating indices of image accuracy. $\delta D = D^{\mathrm{bkgr}} - D^{\mathrm{incl}}$, $\delta D_0$ = maximal value of $\delta D$, $\Delta(\delta D)$ = depth of the notch between the inclusions. $\delta X_0$ = true interinclusion separation distance, $\delta X$ = image interinclusion separation distance.

where $\delta X_0$ is the distance between the inclusion centers in the target medium, and $\delta X$ is the distance between the mesh nodes where $|\delta D|$ is maximal in each inclusion.

It is sometimes useful to express the mean recovered contrast and the FWHM as fractions of the corresponding target-medium values. The terms RM and RW are used to denote relative mean contrast and relative width, respectively.

## 3. Results

### A. Low-Contrast Media

Variations in physiologic state frequently are associated with small changes in tissue light scattering.[11,12] Thus it is useful to investigate the accuracy of diffusion coefficients recovered by the linear reconstruction-and-correction method, as a function of contrast, noise, and inclusion location.

#### 1. *Two-Object Resolving Power*

For the media with purely dynamic inclusions (i.e., $\langle \mu_s'(t) \rangle = \mu_s'^{\mathrm{bkgr}}$), the scattering contrast varies over time, from 0.9 to 1.1. In the two-inclusion cases, because distinct modulation frequencies were modeled, both inclusions are more strongly or more weakly scattering than the background at some time frames, while at others they straddle the background value. These categories are referred to here as *Syn* and *Anti*, respectively. Figure 3 shows examples of uncorrected and corrected images of $\Delta D$ for one *Syn* time frame and one *Anti* time frame. This is an especially challenging case, as the inclusions are located near the center and touch each other.

At the grossest level of inspection, it is seen that the inclusions are not resolved in either the uncorrected [Fig. 3(a)] or corrected [Fig. 3(b)] *Syn* image, while in

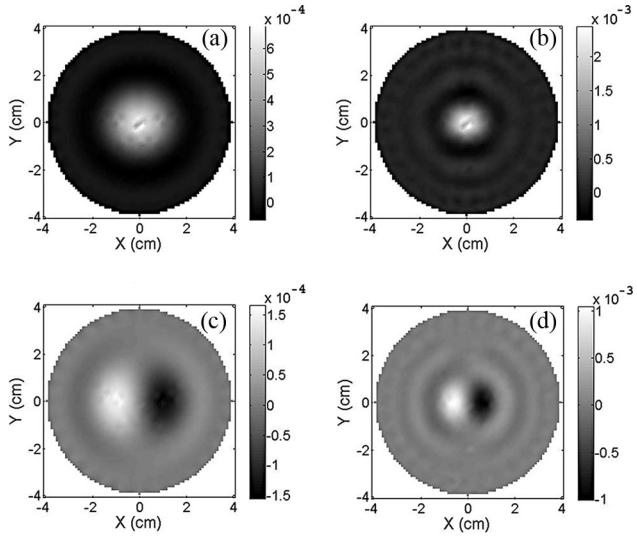


Fig. 3. Low-contrast-medium images, recovered from noise-free data. The 0.6 cm inclusions have a point of contact at $(x, y) = (0, 0)$. (a) Uncorrected image when $\Delta D > 0$ in both inclusions. (b) Corrected image, $\Delta D > 0$ in both inclusions. (c) Uncorrected image, $\Delta D > 0$ in one inclusion, and $<0$ in the other. (d) Corrected image, $\Delta D > 0$ in one inclusion, and $<0$ in the other.

the *Anti* state the inclusions are well resolved even in the uncorrected image [Fig. 3(c)]. However, closer examination reveals that the corrected images are superior in several respects. First, the recovered $\Delta D$ ranges are closer to those actually present in the target medium in the corrected images [$\Delta D_{\text{image}}/\Delta D_{\text{target}} = 0.86$ in Fig. 3(b), 0.36 in Fig. 3(d)] than in the corresponding uncorrected ones [$\Delta D_{\text{image}}/\Delta D_{\text{target}} = 0.24$ in Fig. 3(a), 0.057 in Fig. 3(c)]. Second, the corrected images have higher SC values [0.84 in Fig. 3(b), 0.63 in Fig. 3(d)] than those of the corresponding uncorrected images [0.67 in Fig. 3(a), 0.32 in Fig. 3(c)]. It is noteworthy that the *Anti* images, while showing well-resolved inclusions, are less accurate than the *Syn* images in terms of both quantitative $\Delta D$ recovery and SC value. Third, the corrected images provide better approximations to the true spatial extent of the inclusions even though these are not resolved in Fig. 3(b).

As the distance separating the inclusions is increased, image quality would be expected to increase. Shown in Figure 4 are the uncorrected and corrected images of the two-inclusion low-contrast medium, at a *Syn* time frame, when the inclusion centers are separated by 2 cm. It is seen in Fig. 4(a) that the inclusions are not resolved in the uncorrected image, even though the 1.4 cm gap between them is more than twice as wide as their 0.6 cm diameter. In contrast, the corrected image in Fig. 4(b) reveals the presence of two distinct objects. An inspection of corresponding results (not shown) for intermediate interinclusion distances indicates that they begin to be resolved when the gap between them is wider than their diameter.

The image accuracy indices computed for the results in Fig. 4 and for the corresponding *Anti* images [not shown as the inclusions are already well resolved in Figs. 3(c) and 3(d)] show that the difference between *Syn* and *Anti* image accuracy decreases with increasing separation. The images in Figs. 4(a) and 4(b) have SC values of 0.55 and 0.79, respectively, while the corresponding *Anti* images have SC values of 0.60 and 0.78. As for quantitative accuracy, $\Delta D_{\text{image}}/\Delta D_{\text{target}} = 0.13$ for Fig. 4(a) and 0.55 for Fig. 4(b), and the corresponding *Anti* image values are 0.14 and 0.52. It is interesting that image quality, as measured by these indices, becomes worse for the *Syn* images at the same time as it improves for the *Anti*.

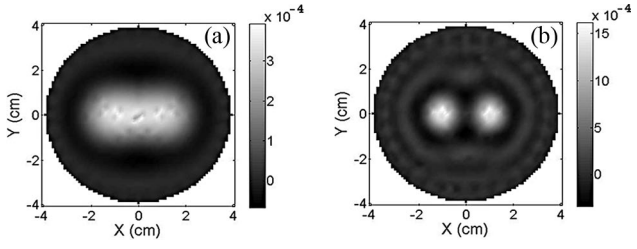


Fig. 4. Low-contrast-medium images, recovered from noise-free data. The distance between the centers of the 0.6 cm inclusions 2 cm. $\Delta D > 0$ in both inclusions. (a) Uncorrected image. (b) Corrected image.

Both trends are suggestive of interactions between the inclusions at small separations. An examination of time-varying SC and $\Delta D_{\text{image}}/\Delta D_{\text{target}}$ data, as a function of separation distance, indicates that these interactions are insignificant when the distance between inclusion centers is $\geq 1$ cm.

### 2. *Contrast–Noise Studies*

Experimental DOT measurement data are not noise-free. Therefore it is important to conduct the type of analysis described above at different levels of data noise, to determine the minimum level of inclusion-to-background contrast that can realistically be recovered. In Fig. 5 we show an example of results from a contrast-titration study, for a fixed noise level of $\varepsilon_k = 1\%$ in all S-D channels. The target medium considered here contained a single inclusion centered at $(x_c, y_c) = (1, 0)$ and 1.2 cm in diameter. Thus we see that the uncorrected-image SC value is weakly dependent on the contrast level, while the corrected-image SC value is strongly contrast dependent. Also there is a threshold contrast value, approximately 1.25 for the specific medium and noise level used here, below which the correction operation degrades the image quality.

Based on the preceding findings, for the balance of this paper we restrict our attention to cases where the inclusion-to-background contrast is either 2 or 3, and to *Syn*-state time frames for two-inclusion results. The former condition guarantees that the contrast threshold is exceeded at all experimentally realistic noise levels, and the latter is the condition for which resolving the inclusions is most difficult.

## B. High-Contrast Media (Noise-Free Data)

### 1. *Single-Inclusion Studies*

The results shown in Figs. 6–9 explore the dependence of image improvement realized by use of the image-correction algorithm, as judged by global and local accuracy indicators, on inclusion size and position. The Fig. 6 results demonstrate the image improvements realized for media having two different inclusion diameters (0.4 cm [Figs. 6(a)–6(c)] and

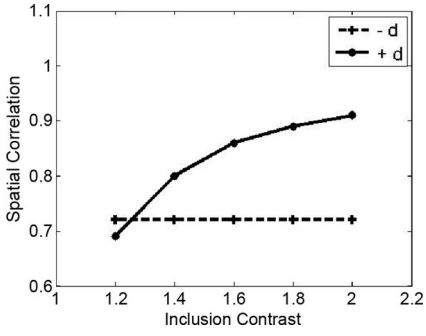


Fig. 5. Plots of spatial correlation value versus scattering-coefficient contrast (i.e., ratio of $\mu_s'$ in the inclusion and background), for uncorrected (dashed line) and corrected (solid curve) images. Target medium contains a single, 1.2 cm diameter inclusion centered at $(x, y) = (1, 0)$. Data noise level is $\varepsilon_k = 1\%$.

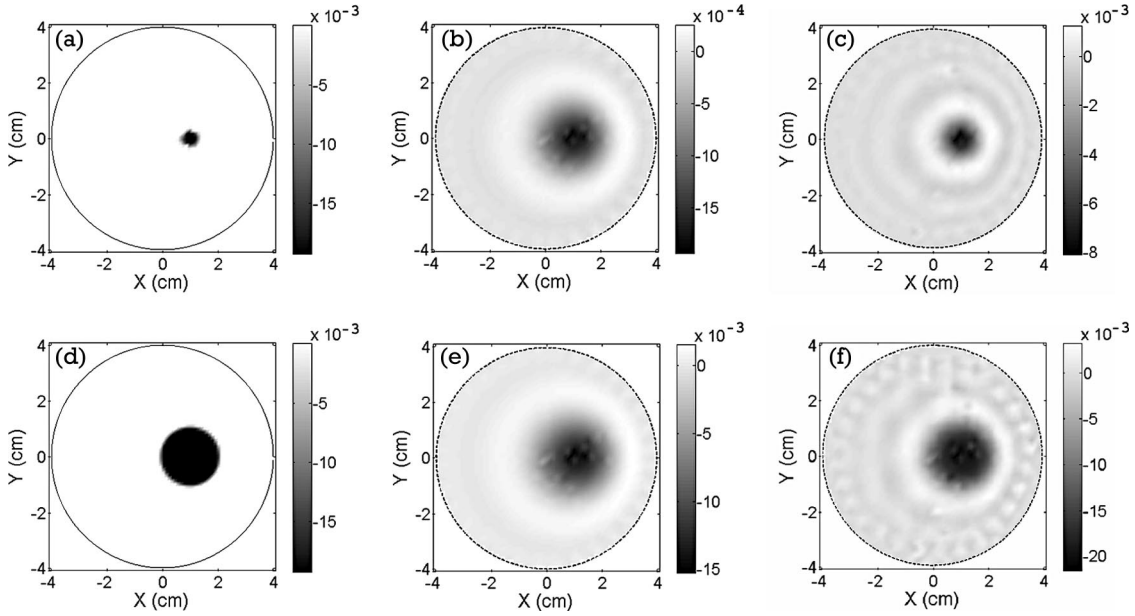


Fig. 6. Representative single-inclusion target media [(a), (d)], uncorrected images [(b), (e)], and corrected [(c), (f)] images. The inclusion is centered at $(x_c, y_c) = (1, 0)$, with diameter of the inclusion is 0.4 cm in (a)–(c), and 2.0 cm in (d)–(f).

2.0 cm [Figs. 6(d)–6(f)]) at a time point where the inclusion contrast is maximal. It is seen that the uncorrected images [Figs. 6(b) and 6(e)] are almost indistinguishable, qualitatively, despite the differences in inclusion diameter. An inspection of the grayscale ranges, however, reveals that there are quantitative differences in the recovered contrast. The corrected images [Figs. 6(c) and 6(f)] provide much better approximations to the true inclusion diameters [Figs. 6(a) and 6(d)], and are more accurate quantitatively.

The noted improvements following image correction would suggest that corresponding improvements should be evident in solutions to the forward problem. This is explored in Fig. 7, which shows the effect of the 0.4 cm diameter inclusion [Figs. 6(a)–6(c)] on the surface detector response, as a function of position about the medium. The results in Fig. 7(a) demonstrate a greatly improved fit to the expected response following image correction, compared to that obtained from the uncorrected image. Shown in Fig. 7(b) is the dependence of the root-mean-squared difference between the observed and expected detector values as a function of source location. An inspection reveals that the corrected image is always more quantitatively accurate. Qualitatively similar results (not shown) were obtained for the large-inclusion case illustrated in Figs. 6(d)–6(f). In quantitative terms, the corrected-image RMSD is even closer to zero here than in Fig. 7(b), while the uncorrected-image results are essentially the same for both the small- and large-diameter inclusions.

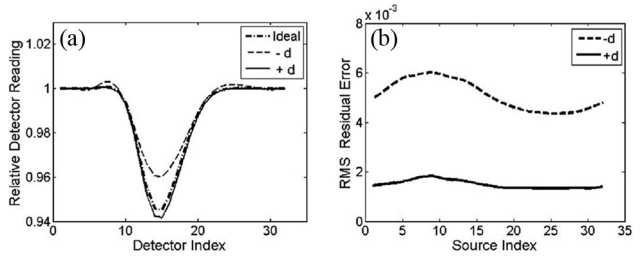


Fig. 7. (a) Normalized detector readings $\eta \equiv R(t)/R^r$, for a source located near the 3 o'clock position in Fig. 1(a), for all 32 detectors at $t = 100$. The dot-dashed curve is computed for the target medium shown in Fig. 3(a). Dashed and solid curves are computed for the images in Figs. 3(b) and 3(c), respectively. (b) Root-mean-squared difference between the $\eta$ curves for the target medium and image (i.e., $\mathrm{RMSD}_i = \left[\sum_{j=1}^{32} (\eta_{ij}^{\mathrm{target}} - \eta_{ij}^{\mathrm{image}})^2/32\right]^{1/2}$, where $i$ and $j$ are the source and detector indices, respectively). Dashed and solid curves are the results for the uncorrected and corrected images, respectively.

The results in Figure 8 explore the dependence of image accuracy improvement on the size and position of the inclusion in the target medium. In Figs. 8(a)–8(c), the size dependence for three different inclusion diameters [Fig. 8(a), 0.4; Fig. 8(b), 1.4; Fig. 8(c), 2.0 cm] is shown. An inspection of the 1D transects through the inclusions, along the $y = 0$ axis, shows that image correction produces improvements in image accuracy in all cases, with the greatest relative improvements realized for the smallest inclusion. Plotted in Figs. 8(d) and 8(e) are the temporal mean values for a local measure of image accuracy (i.e., FWHM), as a function of inclusion size and position. The results in Figs. 8(d) and 8(e) were obtained for inclusions located near the center or near the surface, respectively, as depicted in Fig. 1(b).

An inspection of these data reveals that the FWHM varies with the independent variables in several ways. For instance, the recovered inclusion size is more strongly correlated with the true size after correction than before. It is also seen that image correction substantially removes a recovered inclusion size

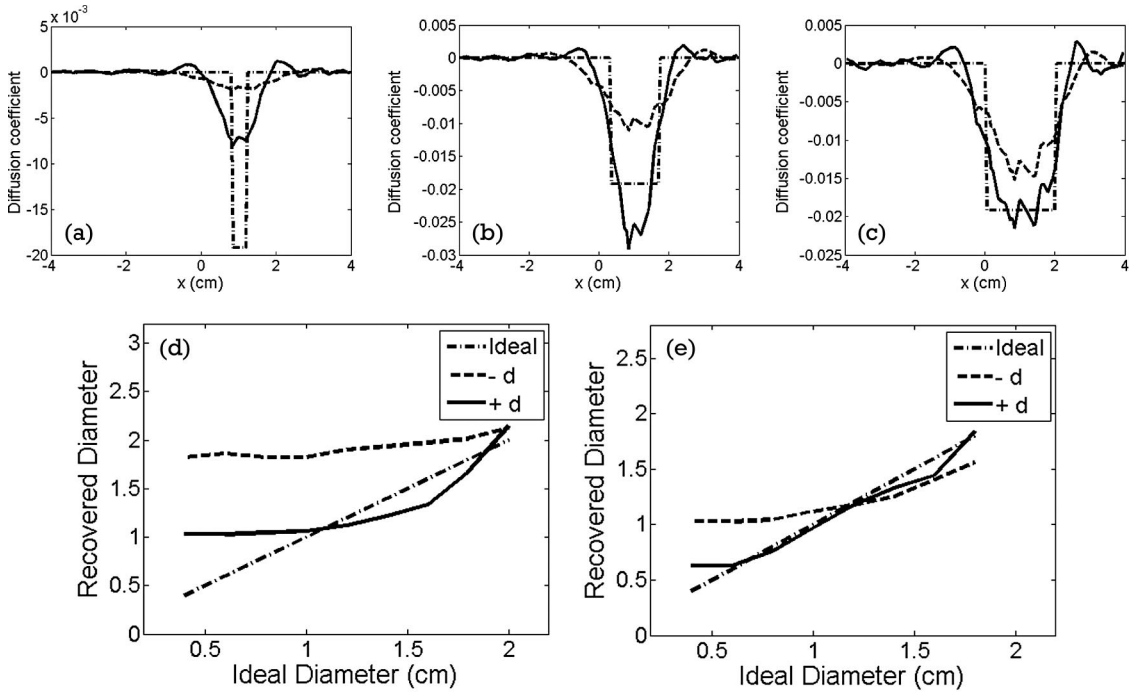


Fig. 8. (a) One-dimensional sections, along the $y = 0$ diameter, through one-inclusion target medium, uncorrected image, and corrected image, for 0.4 cm diameter inclusion [Figs. 3(a)–3(c)]. (b) Analogous 1D sections for a medium with a 1.2 cm diameter inclusion. (c) One-dimensional sections for a medium with a 2.0 cm diameter inclusion [Figs. 3(d)–3(f)]. (d) Recovered versus true inclusion diameter (i.e., FWHM), for the uncorrected and corrected images of all single-inclusion target media with $(x_c, y_c) = (1, 0)$. (e) FWHM of the uncorrected and corrected images, for all $(x_c, y_c) = (3, 0)$ target media. −d = uncorrected images, +d = corrected images.

bias present in the uncorrected images. This is evident in Fig. 8(e), where a crossover point is seen, such that for diameters <1.2 cm the inclusion size is overestimated, while the opposite trend is seen for diameters >1.2 cm. A comparison of results for the inclusion locations shows that greater image accuracy is obtained for those positioned closer to the surface. This holds even for corrected images and is consistent with the expected influence of position-dependent spatial gradients in the weight function. This comparison also shows that the lower size limit for the inclusion, below which overestimates of its size are obtained even with image correction, is 0.6 and 1.05 cm diameter for the outer and inner inclusion positions, respectively.

Other indices of image accuracy are plotted in Fig. 9. In Figs. 9(a) and 9(b), a global accuracy measure is shown (i.e., SC value averaged over all points in the time series). In Figs. 9(c) and 9(d), a local accuracy measure is presented (i.e., tRMSD between true and recovered contrast values, for the image pixels within the boundary of the inclusion). The trends seen are generally consistent with those in Fig. 8: Image correction improves the spatial and temporal measures of image accuracy, with the best results seen for the more superficial inclusion. Interestingly, a comparison of these improvements between the spatial and temporal dimensions shows different trends, with some suggestion that relatively greater improvements are seen upon image correction in the temporal index for smaller inclusion sizes.

*2. Two-Inclusion Studies*

Two different studies were conducted. In one, resolution is explored as a function of object depth (Figs. 10 and 11). In the other, resolution is explored as a function of the distance separating the two inclusions

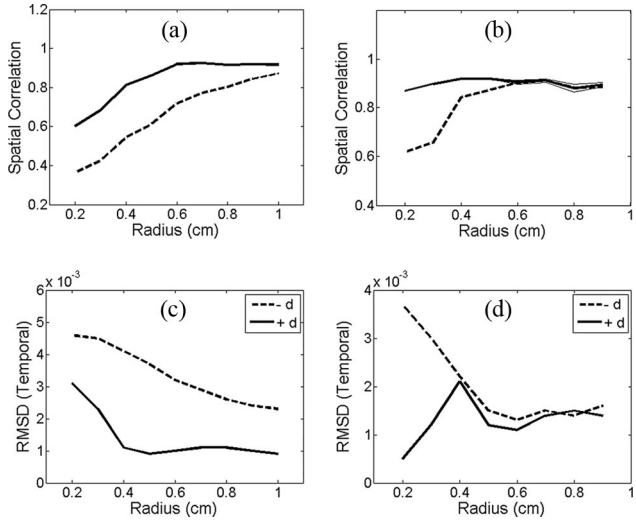


Fig. 9. Spatial correlation [(a), (b)] and temporal RMSD [(c), (d)] accuracy indices, for all single-inclusion target media. The results shown are mean values over 100 time frames. (a), (c) $(x_c, y_c) = (1, 0)$. (b), (d) $(x_c, y_c) = (3, 0)$. Thin lines in (b) are mean ±SD; in the other panels, SD is smaller than the line thickness. −d = uncorrected images, +d = corrected images.

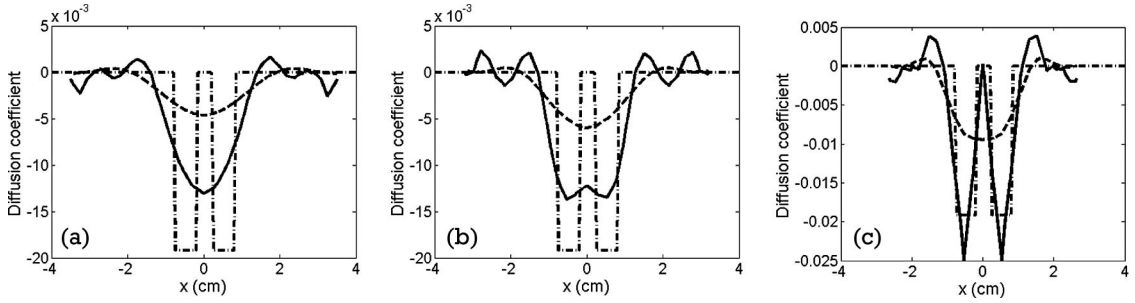


Fig. 10. (a) One-dimensional sections along the line $y = 1$, through a two-inclusion target medium and corresponding images, where $(x_c, y_c) = (\pm 0.5, 1)$. (b) Analogous 1D sections along the line $y = 2$, for the $(x_c, y_c) = (\pm 0.5, 2)$ case. (c) Analogous 1D sections along the line $y = 3$, for the $(x_c, y_c) = (\pm 0.5, 3)$ case. Dot-dashed, dashed, and solid curves are sections through target media, uncorrected images, and corrected images, respectively.

(Fig. 12). It will be recalled that the mean inclusion contrast (i.e., scattering coefficient value) is twice that of the background and is modulated by $\pm 20\%$ at a frequency of 0.1 Hz. In Fig. 10, results are shown for a selected time point at which the inclusion contrast was maximal (2.2× background). The inclusions modeled are centered at $x_c = \pm 0.5$ cm, i.e., the gap separating them is 0.4 cm wide. The $y$ coordinates of the inclusion centers are $y_c = 1$, 2, and 3 cm in Figs. 10(a)–10(c), respectively [cf Fig. 1(c)]. The plotted curves are 1D sections along the line bisecting the inclusion centers. It is seen that even at their most superficial position the pair is never resolved in the uncorrected images, while in the corrected images they are partly resolved when $y_c = 2$ cm and fully resolved when $y_c = 3$ cm (i.e., the most superficial location).

Image accuracy indices for this study, considering results obtained at all time points, are shown in Fig. 11. The resolving-power index $P_d$ is shown as a function of $y_c$ in Fig. 11(a), while the location-bias index $P_s$ is plotted versus $y_c$ in Fig. 11(b). As suggested by the Fig. 10 results, neither index rises above zero for the uncorrected images, indicating that the inclusions are never even partially resolved. For the corrected images, partial resolution is seen when $y_c > 1.4$ cm. For $y_c > 1.4$, the $P_s$ index increases rapidly, reaching the ideal value by the time $y_c = 2$. The $P_d$ index increases monotonically but more slowly, reaching the ideal value of unity only for the most superficial position.

The other quantities plotted in Fig. 11 are counterparts of those in Fig. 9. Heavy curves are mean values over all 100 time frames [Figs. 11(a)–11(c)], or over all

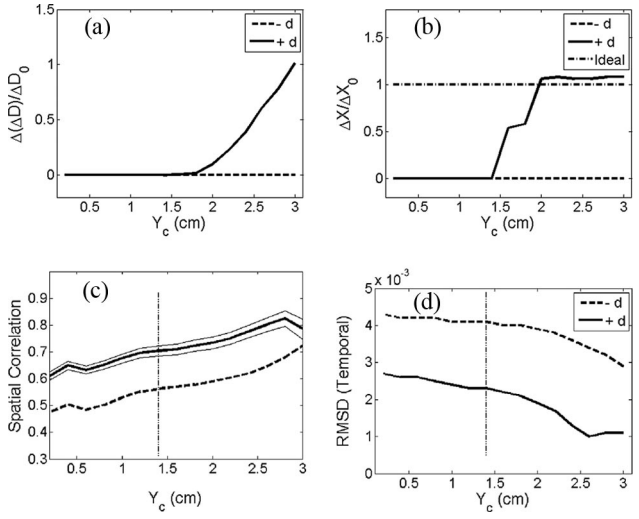


Fig. 11. (a) Resolving-power index $P_d$, as a function of the inclusion-center coordinate $y_c$, for images of the two-inclusion target media considered in Fig. 10 (i.e., $|x_c|$ has a fixed value of 0.5, $y_c$ is variable). (b) Location-bias index $P_s$ versus $y_c$, for the same set of media. (c) Spatial correlation between target medium and image as a function of $y_c$. (d) Temporal RMSD versus $y_c$. Thin lines in (c) are mean ±SD; in the other panels SD is smaller than the line thickness. Vertical dot-dashed lines in (c) and (d) indicate the distance from the center, above which the inclusions can be resolved. −d = uncorrected images, +d = corrected images.

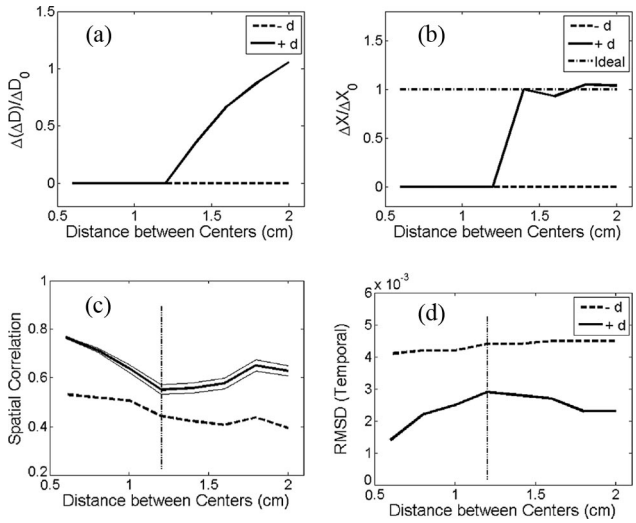


Fig. 12. (a) Resolving-power index $P_d$, as a function of the inclusion-center coordinate $x_c$, for recovered images in the second two-inclusion study (i.e., $x_c$ is variable, $y_c$ has a fixed value of 0). (b) Location-bias index $P_s$ versus $x_c$ for the same set of media. (c) Spatial correlation versus $x_c$. (d) Temporal RMSD versus $x_c$. Thin lines in (c) are mean ±SD; in the other panels, SD is smaller than the line thickness. Vertical dot-dashed lines in (c) and (d) indicate the separation distance, above which the inclusions can be resolved. −d = uncorrected images, +d = corrected images.

FEM mesh nodes within the inclusions [Fig. 11(d)], while the thin curves in Fig. 11(c) are the standard deviation (SD) values about the mean. It is seen that the SC [Fig. 11(c)] is significantly higher, and that the tRMSD [Fig. 11(d)] is substantially lower, in the corrected than in the uncorrected images. The sRMSD (not shown) of the corrected images also is less than or equal to that of the uncorrected images. The vertical dotted lines in Figs. 11(c) and 11(d) are located at the $y_c$ value where the inclusions begin to be resolved. An inspection shows that when the inclusions are more superficial than this depth, the SC grows more rapidly with increasing $y_c$, and the tRMSD falls more rapidly.

Figure 12 shows results analogous to those in Fig. 11, but derived from the complementary study where $y_c = 0$ while $x_c$ was varied from 0.3 cm to 1 cm. As in Fig. 11, heavy curves show mean values over all 100 time frames in Figs. 12(a)–12(c), and mean values over all FEM mesh nodes in the inclusions in Fig. 12(d), while the thin curves in Fig. 12(c) are $\pm$SD values about the mean. Here, too, it is seen that the inclusions are not resolved in the uncorrected images, even at the largest separation distance. In the corrected images they are partially resolved, in terms of the $P_d$ index, as soon as $x_c$ exceeds 0.6 cm [Fig. 12(a)]. The dependence of $P_s$ on separation is even more striking: The value of this index increases from 0

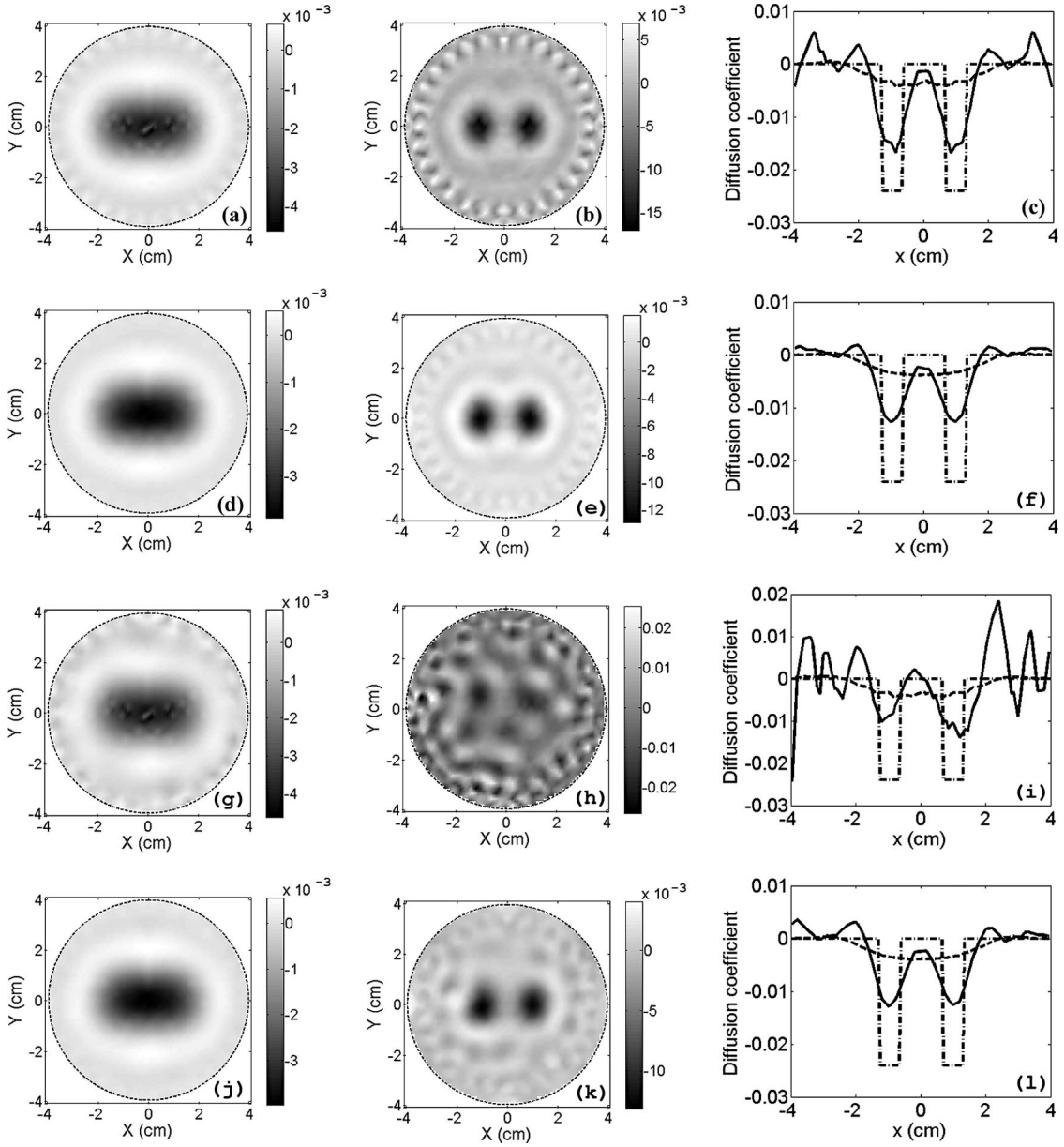


Fig. 13. Recovered images of a two-inclusion target medium, with $(x_c, y_c) = (\pm 0.9, 0)$. (a)–(f) Detector data are noise-free; (g)–(l) detector data noise level is 1%. (a) and (g) uncorrected, unfiltered images; (b) and (h) corrected, unfiltered images; (d) and (j) uncorrected, low-pass filtered images; (e) and (k) corrected, low-pass filtered images. (c), (f), (i), (l) One-dimensional sections through the plotted 2D images along the $y = 0$ diameter.

($x_c \leq 0.6$) to 1 ($x_c > 0.6$) in a single step [Fig. 12(b)]. The $x_c = 0.6$ case has physical significance: It is at this separation that the closest-approach distance is equal to the inclusion diameter.

The dotted vertical lines in Figs. 12(c) and 12(d) demarcate the unresolved from the resolved cases. There are unmistakable differences in the SC versus $x_c$ and tRMSD versus $x_c$ trends on the two sides of the dotted lines. While the corrected image has the larger SC at all values of $x_c$ [Fig. 12(c)], that index initially decreases with increasing $x_c$ (i.e., qualitative accuracy becomes worse), but it begins to increase when $x_c > 0.6$. Similarly, the corrected-image tRMSD [Fig. 12(d)] and sRMSD (not shown) are always less than the corresponding uncorrected values, but they initially grow with increasing $x_c$ (i.e., quantitative accuracy becomes worse). However, the tRMSD falls with increasing separation, and the sRMSD levels off, when $x_c > 0.6$.

### C. Effects of Data Noise (High-Contrast Media)

Representative images from a noise-titration study, involving a two-inclusion target medium, are shown in Fig. 13. The inclusions are centered at $(x_c, y_c) = (\pm 0.9, 0)$, and the noise level of the detector data was either $\varepsilon_k = 0\%$ [Figs. 13(a)–13(f)] or $\varepsilon_k = 1\%$ [Figs. 13(g)–13(l)]. Note that because these inclusions are nearer the center than those considered in Figs. 10 and 11, and noise has been added to the detector data, here we have increased the scattering contrast of the inclusion to a mean value of 3× background, with ±20% amplitude modulation. To improve the achievable image quality, in addition to applying the image-correction operation, we have applied spatial and temporal low-pass filtering to the image time series. As with the results in Fig. 10, the particular case shown is for a time point having maximal contrast relative to the background (i.e., 3.4×). The post-construction operations applied to the data shown in Fig. 13 are: none [Figs. 13(a) and 13(g)]; image correction only [Figs. 13(b) and 13(h)]; low-pass filtering only [Figs. 13(d) and 13(j)]; both [Figs. 13(e) and 13(k)]. Because of differences in quantitative accuracy, the images presented here have different gray-scale ranges. However, a common fixed scale is applied to the plots of 1D sections ($y = 0$) shown in Figs. 13(c), 13(f), 13(i) and 13(l). The latter also provide for straightforward visualization of the smoothness and edge detection quality of each image.

Similar to the findings seen in the preceding sections, an inspection reveals that the corrected images are superior in terms of spatial resolving power, quantitative accuracy, and edge detection. At the same time, however, the correction operation tends to amplify background artifacts, whether they originate from systematic factors [Fig. 13(b)] or from noise [Fig. 13(h)]. The inclusions are recovered with fair accuracy even when the detector data are noisy [Fig. 13(i)], but the amplitudes of noise artifacts can become comparable to those of the inclusions. Using the tLPF and sLPF in combination[5] substantially reduces the background artifacts [compare Figs. 13(b) and 13(e)], at the cost of some reduction in quantitative accuracy [compare Figs. 13(c) and 13(f)]. Results similar to those presented here were obtained for other time frames, for other noise levels in the two-inclusion studies, and in the one-inclusion studies (results not shown).

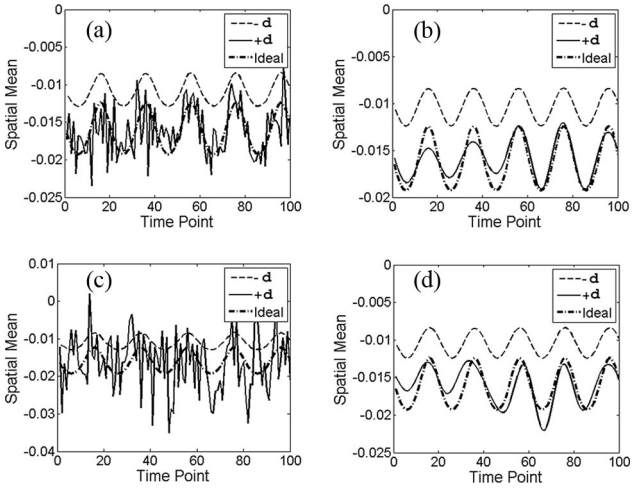


Fig. 14. Spatial mean value of the time-varying $\Delta D$, within the inclusion, for the Fig. 1(b) one-inclusion case. Dot-dashed curves show the true $\langle \Delta D(\mathbf{r}) \rangle$ versus $t$ of the target medium. Dashed curves are the corresponding $\langle \Delta D(\mathbf{r}) \rangle$ versus $t$ plots for uncorrected images. Solid curves are the corresponding plots for the corrected images. (a) and (b) Detector data noise level is 1%. (c) and (d) Detector data noise level is 3%. (a) and (c) Unfiltered image data; (b) and (d) low-pass filtered image data.

Whereas the preceding results concern a single image frame, in Fig. 14 the the effects of image correction, data noise, and noise suppression are summarized for an entire time series. The curves shown were computed for a one-inclusion medium, with $(x_c, y_c) = (1, 0)$ and a 2 cm inclusion diameter. The dot-dashed curves are the average value of $\Delta D$ within the inclusions of the target medium. Dashed and solid curves are the corresponding spatial mean $\Delta D$ in the uncorrected and corrected images, respectively. The noise levels in the detector data used were $\varepsilon_k = 1\%$ [Figs. 14(a) and 14(b)] and 3% [Figs. 14(c) and 14(d)]. Plots of $\Delta D$ versus $t$ are shown both before [Figs. 14(a) and 14(c)] and after [Figs. 14(b) and 14(d)] noise suppression is performed. These complement the single time-frame results in Fig. 13 and show that the correction procedure substantially enhances quantitative accuracy but also amplifies the impact of noise. The noise effect is seen primarily at higher temporal frequencies (just as Fig. 13 shows that it affects predominantly the high spatial frequencies), while the low-frequency inclusion dynamics are recovered with considerable accuracy. The noise-suppression step yields images with high temporal correlations between the target medium and image time series at both noise levels considered.

The performance of the image-correction operation was more extensively characterized by increasing the noise level to a maximum value of $\varepsilon_k = 8\%$. (Owing to the greater impact of noise in 2D computational stud-

Table 1. Indices of Qualitative and Quantitative Spatial Accuracy

| Number of Inclusions | Noise Level[a] | SC[b] | | RM[c] | | RW[c] | |
|---|---|---|---|---|---|---|---|
| | | Uncorrected | Corrected | Uncorrected | Corrected | Uncorrected | Corrected |
| 1 | 0% | 0.87 | 0.93 | 0.65 | 0.96 | 1.23 | 1.05 |
| | 1% | 0.87 | 0.90 | 0.65 | 0.96 | 1.23 | 1.05 |
| | 2% | 0.87 | 0.80 | 0.65 | 0.93 | 1.12 | 1.12 |
| | 3% | 0.87 | 0.70 | 0.65 | 0.87 | 1.12 | 1.07 |
| | 5% | 0.87 | 0.56 | 0.65 | 0.85 | 1.15 | 0.98 |
| | 8% | 0.86 | 0.38 | 0.65 | 0.83 | 1.12 | 1.07 |
| 2 | 0% | 0.43 | 0.65 | 0.14 | 0.49 | – | 1.46 |
| | 1% | 0.43 | 0.62 | 0.14 | 0.48 | – | 1.46 |
| | 2% | 0.43 | 0.48 | 0.14 | 0.47 | – | 1.71 |
| | 3% | 0.43 | 0.35 | 0.14 | 0.40 | – | 1.62 |

[a]The tLPF and sLPF noise-suppression operations are applied to all the reconstructed images.
[b]Spatial correlation computation encompasses the entire FEM mesh.
[c]Relative mean and relative width computations consider only the nodes within the inclusions.

ies[5,13] than in 3D,[6,8] 8% greatly exceeds the noise levels typical of experimental DOT measurement data). The time-averaged SC, RM, and RW values are compiled in Table 1, for representative one-inclusion and two-inclusion target media. (In two-inclusion cases no RW value is reported if the inclusions are not even partially resolved.) The corresponding inclusion-area-averaged TC values are reported in Table 2. The single inclusion was centered at $(x_c, y_c) = (1, 0)$, and its diameter was 2 cm, while the paired inclusions (0.6 cm diameter) were centered at $(x_c, y_c) = (\pm 1, 0)$.

An inspection of these data show that the noise dependence of both correlation values is stronger in the corrected than in the uncorrected images. An uncritical examination of these trends could lead to a mistaken conclusion, that the image correction procedure is beneficial only at very low noise levels. In reality, the SC trend is a largely a consequence of residual background artifacts such as those in Fig. 13(k), and the TC trend is strongly influenced by residual time-varying phase shifts such as those in Fig. 14(d). The RM and RW data in Table 1 indicate that, up to the highest noise level modeled, the sizes and magnitudes of recovered inclusions are more accurate in the corrected images. In experimental and clinical practice, some amount of prior knowledge regarding locations of regions of interest usually is available. This suggests that magnitudes and sizes of diffusion-coefficient perturbations of clinical interest can be recovered from experimental data having realistic noise levels.

Table 2. Temporal Correlation Coefficients

| Number of Inclusions | Noise Level[a] | TC[b] | |
|---|---|---|---|
| | | Uncorrected | Corrected |
| 1 | 0% | 1[c] | 0.999 |
| | 1% | 0.995 | 0.877 |
| | 2% | 0.995 | 0.521 |
| | 3% | 0.995 | 0.484 |
| | 5% | 0.993 | 0.360 |
| | 8% | 0.992 | −0.165 |
| 2 | 0% | 1[b] | 1[b] |
| | 1% | 0.987 | 0.779 |
| | 2% | 0.985 | 0.516 |
| | 3% | 0.980 | 0.420 |

[a]The tLPF and sLPF noise-suppression operations are applied to all the reconstructed images.
[b]Temporal correlation computation considers only the nodes within the inclusions.
[c]TC > 0.9995.

## 4. Discussion

When DOT image recovery is carried out for time-series data, the issue of computational efficiency takes on increased importance. Our recognition of this fact was the motivating factor for this paper and the companion paper (Ref. 8), which report on recent progress relating to the development of a two-stage, linear image reconstruction-and-correction algorithm. Here we have demonstrated that the described method can yield images of diffusion-coefficient perturbations, of a quality comparable to that achieved using more sophisticated reconstruction algorithms, in a small fraction of the time.

The results presented in this paper are substantially similar to those reported in Refs. 3 and 5 for the recovery of $\Delta\mu_a$. A careful comparison reveals some apparent differences in detail (e.g., corrected $\Delta D$ images seemingly have better quantitative accuracy than their $\Delta\mu_a$ counterparts). However, specific conclusions regarding quantitative differences cannot be made yet, because the $\Delta D$ and $\Delta\mu_a$ computations were not conducted with identical FEM meshes or S-D configurations.

### A. Mechanism of Action for the Linear Image Correction Algorithm

A point illustrated in Refs. 4 and 8 is that the use of the correction procedure yields improvements in image accuracy, regardless of the value chosen for the Tikhonov regularization parameter. Those demonstrations effectively refute the suggestion that the lower quality of uncorrected images is a simple consequence of selecting the wrong parameter value. But

in doing so, they raise other significant questions: What, then, is the basis of the correction method's effectiveness? How is it different from standard regularized image reconstruction methods?

The various approaches to DOT image reconstruction[14] differ in many details but have an essential feature in common. Namely, the principal criterion for successful image reconstruction is close agreement between the measurement data and a computed solution to the forward problem. As the inverse problem typically is underdetermined, there can be uncertainty as to the quantitative accuracy of the result. The conventional response to this is to incorporate some form of regularization into the inverse problem.[15] Regularization has the effect of limiting the set of admissible inverse-problem solutions to those that satisfy some type of assumption regarding the optical coefficients of the medium. Typically used assumptions are: The correct solution, or one of its spatial derivatives, is continuous (Tikhonov regularization)[16]; minimum and maximum possible values for the optical coefficients are known (range constraints[9]); the solution is band limited, with known minimum and maximum spatial frequencies (truncated singular value decomposition,[17] discrete-cosine transform[18]); or the spatial distribution of optical coefficients closely follows anatomy (structural priors[19]).

The linear image correction method used here differs from conventional regularization strategies in an important way. A computation of a correction matrix entails a direct comparison between a large number of known, uncorrelated medium states and the corresponding uncorrected images.[3–5] Thus additional information, of a type not available to the standard approaches, is introduced into the inverse problem. The process used to generate the correction matrix may be thought of as a form of regularization. However, the information that is distilled into the correction matrix is precisely tailored to the particular mesh and reference medium used. It follows that the correction is not simply equivalent to any of the regularization methods listed above, which do not incorporate an equivalent amount of medium-specific information. Therefore, it is not surprising that the image quality achieved here and in previous reports cannot be replicated simply by, for example, adjusting the value of a Tikhonov regularization parameter.[4]

### B. Future Directions

The studies conducted for this report lay the groundwork for exploring an idea first outlined in Ref. 4, for reducing interparameter cross talk in DOT images. This would be accomplished by simultaneously modulating $\mu_a$ and $D$ of the reference medium, then computing correction matrices from the known medium states and their corresponding (uncorrected) reconstructed images. The underlying assumption, which the computations will directly test, is that misidentification of one optical coefficient as the other by a reconstruction algorithm is analogous to the blurring and location bias errors that are considered in this paper.

A successful outcome to the preceding effort would permit us to consider the possibility of combining the image-reconstruction and image-correction operators into a single matrix. When images are reconstructed using the NDM, both the $\Delta\mu_a$ and $\Delta D$ perturbations are solved for simultaneously. Formally

$$\underbrace{[\mathbf{W}_{\mu_a}|\mathbf{W}_D]}_{\mathbf{W}}\begin{bmatrix}\Delta\boldsymbol{\mu}_a{}^u\\ \Delta\mathbf{D}^u\end{bmatrix}=[\Delta\mathbf{R}]\Rightarrow\begin{bmatrix}\Delta\boldsymbol{\mu}_a{}^u\\ \Delta\mathbf{D}^u\end{bmatrix}=\underbrace{\begin{bmatrix}\mathbf{X}_{\mu_a}\\ \mathbf{X}_D\end{bmatrix}}_{\mathbf{X}}[\Delta\mathbf{R}], \quad (3)$$

where $\mathbf{X}$ is the (regularized) pseudoinverse of the weight matrix $\mathbf{W}$,[1] and the superscript $u$ denotes the uncorrected image. If a two-coefficient correction matrix were available, it would be straightforward to generate a composite operator that computes corrected images from detector data in a single step, as

$$\begin{bmatrix}\Delta\boldsymbol{\mu}_a{}^c\\ \Delta\mathbf{D}^c\end{bmatrix}=\underbrace{\left[\begin{array}{c|c}\mathbf{F}_{\mu_a\mu_a} & \mathbf{F}_{\mu_aD}\\ \hline \mathbf{F}_{D\mu_a} & \mathbf{F}_{DD}\end{array}\right]}_{\mathbf{F}}\begin{bmatrix}\mathbf{X}_{\mu_a}\\ \mathbf{X}_D\end{bmatrix}[\Delta\mathbf{R}]\equiv\underbrace{\begin{bmatrix}\mathbf{Y}_{\mu_a}\\ \mathbf{Y}_D\end{bmatrix}}_{\mathbf{Y}}[\Delta\mathbf{R}], \quad (4)$$

where $\mathbf{Y} = \mathbf{FX}$, and the superscript $c$ denotes the corrected image. Note that the $\mathbf{F}_{\mu_aD}$ submatrix specifies how to redistribute information from the uncorrected $\Delta D$ image into the corrected $\Delta\mu_a$ image, and that analogous interpretations apply to the other submatrices of $\mathbf{F}$. Additionally, the pseudoinverse of $\mathbf{Y}$ could be interpreted as a corrected weight matrix. This would be a more accurate representation, than first-order perturbation theory provides, of the relation between the medium optical coefficients and the measurement data. As a practical matter, the single-step image formation process represented in Eq. (4) may yield further improvements in image accuracy, by avoiding the accumulation of numerical errors that is often associated with the generation of intermediate results.

Another goal, also directed to further improving corrected image accuracy, will be to reduce the impact of data noise on the fidelity of temporal information recovery. Two possible routes for accomplishing this can be explored. One approach is to incorporate some form of temporal regularization into the image reconstruction algorithm,[20] in contrast to the currently employed strategy of treating each time frame as an independent inverse problem. The former strategy is more computation intensive but is also sensible, as the optical coefficients of a medium would not be expected to change radically on the subsecond time scale of our time-series DOT measurements. The second approach is to incorporate measurement noise directly into the data used for the generation of the correction matrix. Preliminary calculations have shown that this can have the effect of homogeneously redistributing an image's noise component over the entire area or volume of the medium. At the same time, the average noise magnitude per FEM mesh node falls by a factor of $1/\sqrt{N}$, where $N$ is the number

of nodes. The two strategies outlined here are not, of course, mutually exclusive.

Finally, an important assumption underlying the linear correction approach is that the relation between the medium state and the uncorrected image is the same for a physical target medium as for the simulated medium used in the correction matrix computations. To determine if the image correction strategy can be successfully applied to experimental data, we have constructed and performed initial tests on a series of solid-state dynamic phantom media. Preliminary experiments thus far conducted have shown the same types of image quality improvement as are found in simulation studies.[21] The results presented here and in the companion paper will be used in future work aimed at developing phantom media having more complex backgrounds as well as independently variable scattering and absorption. The latter are expected to provide information useful for achieving the ultimate goal of time-series DOT imaging in human subjects, with clinically useful levels of spatial and dynamic accuracy.

This work was supported by the National Institutes of Health (NIH) under grants R21-HL67387, R21-DK63692, R41-CA96102, R41-NS050007, and R43-NS49734, and by the U.S. Army under grant DAMD017-03-C-0018.

### References

1. Y. Pei, H. L. Graber, and R. L. Barbour, "Influence of systematic errors in reference states on image quality and on stability of derived information for DC optical imaging," Appl. Opt. **40,** 5755–5769 (2001).
2. S. R. Arridge and J. C. Hebden, "Optical imaging in medicine II: Modelling and reconstruction," Phys. Med. Biol. **42,** 841–853 (1997).
3. R. L. Barbour, H. L. Graber, Y. Xu, Y. Pei, and R. Aronson, "Strategies for imaging diffusing media," Transp. Theory Stat. Phys. **33,** 361–371 (2004).
4. H. L. Graber, Y. Xu, Y. Pei, and R. L. Barbour, "Spatial deconvolution technique to improve the accuracy of reconstructed three-dimensional diffuse optical tomographic images," Appl. Opt. **44,** 941–953 (2005).
5. Y. Xu, H. L. Graber, Y. Pei, and R. L. Barbour, "Improved accuracy of reconstructed diffuse optical tomographic images by means of spatial deconvolution: two-dimensional quantitative characterization," Appl. Opt. **44,** 2115–2139 (2005).
6. Y. Xu, Y. Pei, H. L. Graber, and R. L. Barbour, "Image quality improvement via spatial deconvolution in optical tomography: Time-series imaging," J. Biomed. Opt. **10,** 051701 (2005).
7. D. W. McRobbie, E. A. Moore, M. J. Graves, and M. R. Prince, MRI from Picture to Proton, 2nd ed. (Cambridge U. Press, 2006.)
8. Y. Xu, H. L. Graber, and R. L. Barbour, "Image correction algorithm for functional three-dimensional diffuse optical tomography brain imaging," Appl. Opt. **46,** 1693–1704 (2007).
9. Y. Pei, H. L. Graber, and R. L. Barbour, "Normalized-constraint algorithm for minimizing inter-parameter cross talk in DC optical tomography," Opt. Express **9,** 97–109 (2001).
10. H. L. Graber, Y. Pei, and R. L. Barbour, "Imaging of spatio-temporal coincident states by DC optical tomography," IEEE Trans. Med. Imaging **21,** 852–866 (2002).
11. B. Chance, P. Cohen, F. Jöbsis, and B. Schoener, "Intracellular oxidation-reduction states *in vivo,*" Science **137,** 499–508 (1962).
12. J. S. Maier, S. A. Walker, S. Fantini, M. A. Franceschini, and E. Gratton, "Possible correlation between blood glucose concentration and the reduced scattering coefficient of tissues in the near infrared," Opt. Lett. **19,** 2062–2064 (1994).
13. B. W. Pogue, T. O. McBride, U. L. Osterberg, and K. D. Paulsen, "Comparison of imaging geometries for diffuse optical tomography of tissue," Opt. Express **4,** 270–286 (1999).
14. A. P. Gibson, J. C. Hebden, and S. R. Arridge, "Recent advances in diffuse optical imaging," Phys. Med. Biol. **50,** R1–R43 (2005).
15. D. Colton, H. W. Engl, A. K. Louis, J. R. McLaughlin, and W. Rundell, eds., Surveys on Solution Methods for Inverse Problems (Springer, 2000).
16. A. N. Tikhonov and V. Y. Arsenin, Solutions of Ill-Posed Problems (V. H. Winston, 1977).
17. P. Xu, "Truncated SVD methods for discrete linear ill-posed problems," Geophys. J. Int. **135,** 505–514 (1998).
18. X. Gu, J. Masciotti, and A. H. Hielscher, "Parametric reconstruction method in optical tomography," in Proceedings of 28th IEEE EMBS Annual International Conference (IEEE, 2006), Paper FrB13.4.
19. M. Huang and Q. Zhu, "Dual-mesh optical tomography reconstruction method with a depth correction that uses *a priori* ultrasound information," Appl. Opt. **43,** 1654–1662 (2004).
20. M. J. Cassidy and W. D. Penny, "Bayesian nonstationary autoregressive models for biomedical signal analysis," IEEE Trans. Biomed. Eng. **49,** 1142–1152 (2002).
21. R. L. Barbour, H. L. Graber, Y. Xu, Y. Pei, R. Ansari, M. B. Levin, and M. Farber, "Diffuse Optical Tissue Simulator (DOTS): An experimental calibrating system for functional DOT imaging," in *Proceedings of Fifth Inter-Institute Workshop on Optical Diagnostic Imaging from Bench to Bedside* (National Institutes of Health, 2006), Poster No. 76.